Materials & Design 237 (2024) 112592

Contents lists available at ScienceDirect

Materials & Design

journal homepage: www.elsevier.com/locate/matdes

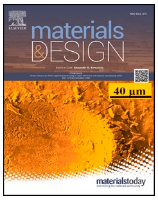

Fracture and Toughening of Mycelium-based Biocomposites

Precious O. Etinosa [a], Ali A. Salifu [b], Sarah Osafo [a,c], Stanley C. Eluu [d], John D. Obayemi [a,e], Winston O. Soboyejo [f,*]

[a] Department of Mechanical and Materials Engineering, Worcester Polytechnic Institute, 100 Institute Road, Worcester, MA 01609, USA
[b] Department of Engineering, Boston College, Chestnut Hill, MA 02467, USA
[c] Department of Materials Science and Engineering, School of Engineering, University of Ghana, Ghana
[d] Department of Pharmaceutical Microbiology and Biotechnology, Faculty of Pharmaceutical Sciences, Nnamdi Azikiwe University, Anambra State, Nigeria
[e] Department of Biomedical Engineering, Worcester Polytechnic Institute (WPI), WPI Life Science and Bioengineering, 60 Prescott Street, Worcester, MA 01609, USA
[f] Department of Engineering, SUNY Polytechnic Institute, 100 Seymour Road, Utica, NY 13502, USA

ARTICLE INFO

Keywords:
Crack-microstructure interactions
Fracture mechanics
Fracture modes
Mycelium-based biocomposites
Resistance-curve behavior
Toughening mechanisms

ABSTRACT

This study presents a combined experimental and analytical study of the fracture behavior and toughening mechanisms of bioprocessed mycelium-based biocomposites. The composites comprise hemicellulose hemp ducts (as nutritional and reinforcing components) intertwined with increasing weight percentages of laterite particles. Single-edge notched fracture experiments and *in-situ* observations of crack growth were used to explore the effects of varying proportions of laterite on the composite resistance-curve behavior. The toughening mechanisms, fracture modes, and crack-microstructure interactions were also elucidated. Since crack-bridging and crack-deflection were observed to be the dominant toughening mechanisms, they were modeled using fracture mechanics approaches. Crack-bridging was shown to dominate the toughening at lower weight fractions of laterite (0–20 wt%). However, as the laterite content increases (20–40 wt%), a combination of crack-bridging and crack-deflection was observed. Finally, at higher laterite weight fractions (>40 wt%), crack-tip shielding occurred primarily via crack deflection. The fracture mechanics predictions of resistance-curve behavior are shown to be consistent with the experimental measurements. The results suggest that mycelium-based and mycelium-laterite composites can be engineered with tunable fracture toughness. The implications of the results are also discussed for the development of sustainable building materials.

1. Introduction

Modern research efforts are focusing on materials production and engineering concepts to incorporate sustainability within the motif of biodegradation [1,2]. Depletion of fossil fuels, problems of synthetic plastics, and environmental nondegradation are presently global concerns [3–5]. These considerations are now motivating sustainability design and materials-related research toward natural-based materials with renewable resources. For example, in the cement construction industry, the energy demand and carbon footprint are rising due to the growing global population and acceleration of urbanization in developing countries [6,7].

The realization of long-term sustainability goals is highly dependent on using renewable materials that minimize CO_2 emissions, embodied energy, and end-of-life wastes [8]. There have been considerable efforts in the development of bio-based materials from naturally available resources, including cellulose and lignin from plant biomass [9], polyesters from bacteria [10,11] proteins from plants [12,13] and animal membranes [14,15]. These materials offer the unique advantages of sustainability, biodegradability, and low-embodied energy requirement with a wide variety of interesting properties [1,16,17].

Mycelium-based biomaterials are new potential alternative materials that have attracted increased research interest in the past decades [18]. The biomaterial is based on the nutritional ability of saprophytic fungi to digest and cement lignocellulosic particles into rigid products [2,19]. This material has properties that are readily tunable and controllable during the growth process [2]. The mycelium composite is a multiscale structure of lignocellulosic reinforcing particles embedded within random mycelium fibrous networks. The chemical compositions of widely used mycelium (*Pleuratus Ostreatus*) and hemicellulose-rich reinforcing particles (hemp) are presented in Tables 1 and 2, respectively. The mycelium matrix is highly porous, composed of about 90 %

---

* Corresponding author.
E-mail address: soboyew@sunypoly.edu (W.O. Soboyejo).

https://doi.org/10.1016/j.matdes.2023.112592
Received 1 November 2023; Received in revised form 12 December 2023; Accepted 17 December 2023

Table 1
Chemical composition of fresh Pleuratus Ostreatus [20].

Chemical composition	Typical range (%)	
	Wet weight	Dry weight
Moisture	86.3	–
Protein	4.67	34.09
Total carbohydrates	6.43	46.94
Ash	1.42	10.36
Lipids	0.21	1.53
Fibers	0.97	7.08

Table 2
Chemical composition of hemp fibers [21–24].

Components	Typical range
Lignin (wt.%)	55–90
Hemicellulose (wt.%)	15–22.4
Cellulose (wt.%)	4–13
Pectin (wt.%)	0.8–1.6
Ash (%)	0.8
Moisture (wt.%)	9–12
Waxes (wt.%)	7–34
Biomass (Mg DM/ha/y)	0.8

moisture, Table 1. The heterogeneous distribution of particles within the porous and random mycelium network makes the composite properties sensitive to material geometry and dimensions.

Our recent study [1] showed that mycelium-hemp composites exhibited unique properties in uniaxial compression dependent on the specimen geometry. Slender beams (aspect ratio of 4:1) undergo global buckling phenomena dominated by the matrix shear and fiber–matrix detachment at higher loads. Whereas in thick beams (aspect ratio of 2:1), the deformation behavior is comparable to that of an open cell structure and soft materials [1]. The composite exhibits an initial linear-elastic regime (~8% strain) followed by a linear strain-hardening domain and then undergoes continuous densification at higher loading [1]. Introducing laterite particles changes the failure mode of the composite to that expected in unidirectional composites, varying the compressive strengths from 250 to 750 kPa [1].

Few studies have investigated the mechanics of deformation of mycelium composite. Aiduang et al. [25] studied mycelium composites and the effects of different fungal species as well as agro-waste residues on the mechanical properties of the resulting composites. They developed composites with compressive strengths ranging from 250 to 1710 kPa and tensile strengths from 200 to 870 kPa. Islam et al. [26] reported lower compressive yield strengths on the order of 40–80 kPa, with ultimate tensile strengths in the range of 100–300 kPa. Travaglini et al. [27] developed a woodchip-mycelium composite with a density of 318 kg/m^3 and reported yield strength of 47.5 kPa in compression. Although these studies provide useful insights into the mechanical properties of mycelium composites, there is limited fundamental understanding of the fracture and toughening mechanisms of mycelium composites.

This study presents the results of a combined experimental and theoretical study of fracture, resistance-curve behavior, and toughening mechanisms of bioprocessed mycelium composites. Fracture toughness is studied using single-edge notched bend specimens (SENBs). A combination of *in-situ* optical microscopy and resistance-curve predictions are used to study the underlying toughening mechanisms associated with resistance-curve behavior. The measured resistance curves are compared with the predictions from theoretical fracture mechanics models. Finally, the implications of the current work are discussed for the design of mycelium and mycelium-laterite composites for potential applications in sustainable buildings.

2. Materials and experimental methods

2.1. Materials

The mycelium strain (*Pleuratus Ostreatus –white oyster mushroom)* and hemp hurds were obtained from Ecovative Design, LLC, Green Island, NY, USA. The oyster mushroom possesses dense mycelium, rapid growth, and easy culture conditions [1]. The chemical compositions of the mycelium and the reinforcing hemp hurds are presented in Tables 1 and 2. The hemp is rich in hemicellulose and functions as a high nutritional reinforcement (Table 2). Red laterite particles were obtained from Tamale Technical University, Ghana.

2.2. Experimental methods

2.2.1. Materials processing

The sample preparation is based on mycelium spores and hemp hurds. Here, the hibernated vegetative spores of the fungi in the presence of the hemp hurds are reactivated in a filter patch bag with nutritional supplements (calcium and carbohydrates). The inoculum is allowed to grow for five days in a sterile and controlled environment (25 °C and relative humidity of 60 %). Then, the inoculated mass is broken into pieces to redistribute the mycelium growth and mixed with laterite particles to achieve varying weight fractions (0–70 wt%). For the remaining sections of this manuscript, specimens with 0, 10, 20, 40, 60, and 70 wt% of laterites will be designated as MHC–0, MHC–10, MHC–20, MHC–30, MHC–40, MHC–60, and MHC–70, respectively. The blended mix is resupplied with nutrients to facilitate the fungal growth and then packed into rectangular molds (30 × 10 × 5 cm) to grow for five additional days. The fully grown mycelium bricks are air-dried for 48 h, then heat-treated at 80 ℃ for 50 min to deactivate the fungal growth and render the sample biologically inactive.

2.2.2. Scanning electron microscopy and energy dispersive x-ray spectroscopy

The microstructural details of the composite and the elemental distribution of the laterite were studied using a scanning electron microscope (SEM) equipped with an Oxford Energy Dispersive Spectroscopy (EDS) system for elemental analysis (JEOL, JSM-700F Field Emission Scanning Electron Microscope, Tokyo, Japan). The SEM specimens were coated with gold/palladium (60:40) at an average density of 17 g/m^3 using a current of 20 mA (EMS/Quorum 150R ES Sputter Coater, East Sussex, England). Then, they were imaged using an accelerating voltage of 10 kV with a spot size of 5 at an average working distance of 10 mm.

The elemental details of the laterite particles were captured using an attached energy-dispersive X-ray spectrometer, and the spectra were analyzed using AZtecEnergy EDS software. An average spectrum is collected for each specimen based on individual spectra obtained from 10 different sites.

2.2.3. Mechanical characterization and resistance-curve experiments

The resistance-curve experiments were carried out using an Instron 8872 servo-hydraulic system (Instron 8872, Instron, Norwood, Massachusetts, USA) equipped with a load cell capacity of 1 kN. The SENB specimen was loaded monotonically in incremental stages until a fracture occurred. Fig. 1 shows a schematic of the specimen. A loading rate of 0.5 mm/min was used, corresponding to a stress-intensity-factor (K) increase rate of 0.01 kPa $\sqrt{\mathrm{m}}/\mathrm{min}$. The crack-tip opening displacements were captured *in-situ* using a proscope digital microscope (Proscope HR, Bodelin Technologies, Oregon, USA) and a digital video camera (Sony, Model FDR-AX33, Japan). The crack-tip displacements and the corresponding applied loads were then plotted into a load-extension curve.

The curve was analyzed using the 95 % secant method to identify the apparent peak load (P_Q) for toughness calculations [28,29]. The conditional value of the fracture toughness (K_Q) was determined from P_Q

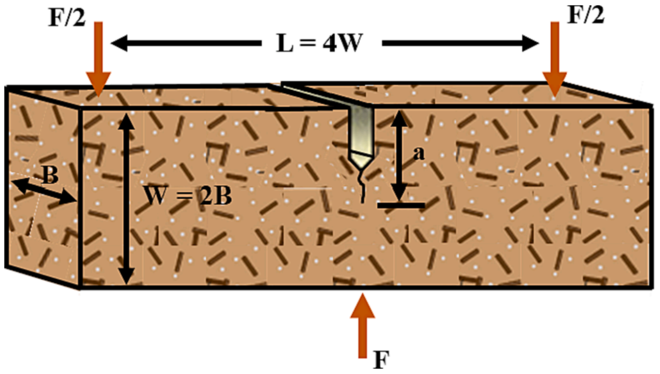

Fig. 1. Schematic of fracture toughness testing of single-edge notched bend specimen of mycelium-hemp composite.

according to Eq. (1). The equation relates P_Q, crack length (a), and the three-point specimen geometry (given in Fig. 1):

$$K_Q=\frac{P_Q S f\left(\frac{a}{W}\right)}{BW^{1.5}} \tag{1}$$

where $f(a/w)$ is a compliance function that is adopted from ASTM E399-90 [30] as follows:

$$f\left(\frac{a}{W}\right)=\frac{3\left(\frac{a}{W}\right)^{\frac{1}{2}}}{2\left(1+2\frac{a}{W}\right)\left(1-\frac{a}{W}\right)^{\frac{3}{2}}}\times\left[1.99-\left(\frac{a}{W}\right)\left(1-\frac{a}{W}\right)\left(2.15-3.93\frac{a}{W}+2.7\frac{a^2}{W^2}\right)\right] \tag{2}$$

Eq. (3) presents the critical conditions to ensure a highly triaxial/plane strain state at the crack tip for which the critical stress intensity factor is accepted as the fracture toughness (plane strain fracture toughness, K_{IC}). K_{IC} is a material property independent of the specimen thickness. The equation is given as follows [30]:

$$B, W < 2.5\left(\frac{K_Q}{\sigma_y S}\right)^2 \tag{3a}$$

$$(W-a) < 2.5\left(\frac{K_Q}{\sigma_y S}\right)^2 \tag{3b}$$

Where B, W, and a are geometric dimensions illustrated in Fig. 1, and σ_y is 0.2 % yield strength. The test is considered valid and the measured conditional K_Q is taken as the material fracture toughness K_{IC} if Eq. (3) holds true and $P_Q \geq 1.1\ P_{max}$ [28,31]. Otherwise, K_Q is considered an apparent fracture toughness.

3. Micromechanical modeling

3.1. Crack toughening mechanism

Toughening typically occurs when propagating cracks undergo crack-tip shielding in which the effective stresses are reduced. Depending on composition and crack microstructural interactions, there are different forms of toughening such as twin, transformation, crack-tip blunting, crack trapping, microcrack shielding/anti-shielding, crack crazing, crack deflection, and crack bridging [28]. Crack bridging and deflection are prevalent in fiber- and particle-reinforced composites [28]. Fig. 2 presents a schematic of crack deflection and bridging.

3.1.1. Toughening due to crack bridging

Toughening due to crack bridging was consistently observed in the resistance-curve experiments. Hence, a micromechanical bridging model is used to analyze the contribution to the toughening mechanism of the composite. The model was explored for small-scale bridging (SSB) and large-scale bridging (LSB) [28,32]. The SSB model is presumed to be accurate for crack length $\Delta a < \sim 0.5$ mm, while the LSB model is considered to provide better predictions for crack length ≥ 0.5 mm [33].

SSB conditions were observed at the early stages of loading as the crack fronts opened. An elastic–plastic spring model (Fig. 2a) has been used by Li and Soboyejo [34] and Budiansky [32] to idealize toughening due to small-scale bridging. The toughening contribution can be estimated in terms of the maximum stress intensity factor (ΔK_{SSB}) the sample can sustain before fracture [35]. This is expressed in Eq. (4) [28].

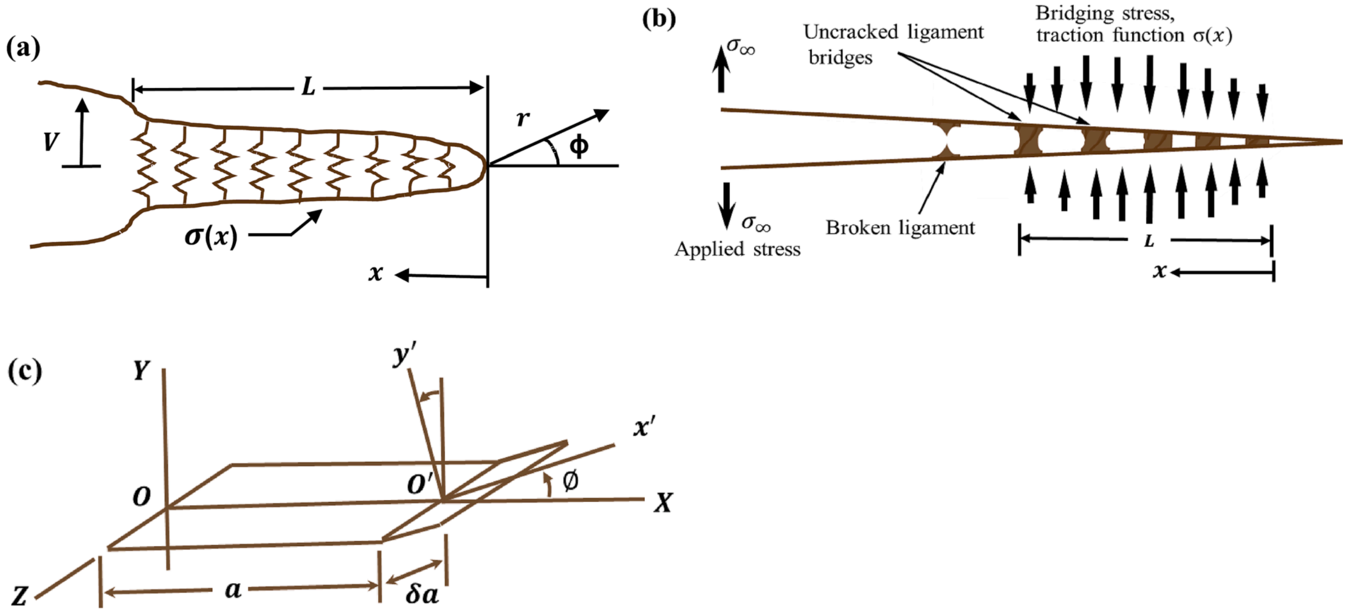

Fig. 2. Schematic of toughening mechanisms due (a) small-scale crack bridging illustrated by a spring model (b) weighted distribution of traction forces across bridging ligaments in large-scale crack bridging (c) crack deflection by pure tilting.

$$\Delta K_{SSB} = \alpha V_f \sqrt{\frac{2}{\pi}} \int_0^L \frac{\sigma_y}{\sqrt{x}} dx \tag{4}$$

where α is the constraint/triaxiality parameter to finetune the model (typically of a value between 1 and 3) [36,37], V_f is the volume fraction of the bridging ligaments along the crack, σ_y is the uniaxial yield stress, L is the bridging length (taken as the horizontal distance between the crack tip and the last unfractured ligament), and x is the distance from the crack tip or the remaining distance behind the crack tip (Fig. 2a) [35].

In the case of LSB, the toughening increment (ΔK_{LSB}) can be estimated using a model that constitutes a weighting traction function, as described by Fett and Munz [38]. The model is simplified to estimate the weighted distributions of bridging traction across the toughening domain, Fig. 2b [34,39,40]. ΔK_{LSB} is expressed in Eq. (5).

$$\Delta K_{LSB} = \alpha V_f \int_L^{\cdot} \sigma_y h(a,x) dx \tag{5}$$

where *h(a, x)* is the weighting function for the bridging tractions and the expression is given by Fett and Munz [38] to be:

$$h(a,x) = \sqrt{\frac{2}{\pi a}} \frac{1}{\sqrt{1-\frac{x}{a}}} \left[1 + \sum_{(v,\mu)} \frac{A_{v,\mu}\left(\frac{a}{w}\right)}{\left(1-\frac{a}{w}\right)} \left(1-\frac{x}{a}\right)^{v+1} \right] \tag{6}$$

where the coefficients $A_{v,u}$ for SENB specimen are summarized in Table 3.

The overall toughness of the fiber-reinforced composite (K_C) can be expressed as the sum of the initiation toughness (K_i) and the toughening component due to the crack bridging (ΔK_B). The expression is given in Eq. (7).

$$K_C = K_i + \Delta K_B \tag{7}$$

$\Delta K_B = \Delta K_{SSB}$ and ΔK_{LSB} for short-scale and long-scale bridging, respectively.

3.1.2. *Toughening due to crack deflection*

Crack deflections were observed as the prevalent toughening mechanism in specimens with laterite content greater than 40 wt%. Schematics of crack-deflections is provided in Fig. 2c. The laterite particles at the crack front of an advancing crack deflect the crack path. Bilby et al. [41] and Cotterell and Rice [42] developed an approach to explain the role of in-plane crack tilting/deflection and out-of-plane twisting in crack-tip shielding. Deflection-induced shielding due to pure tilting through an angle (ϕ) can be estimated from the Modes I and II stress intensity factors, K_I and K_{II}[43]. When the crack consists of equal deflected and undeflected segments, K_I and K_{II} may be estimated using simple geometrical expressions according to Suresh [43]. These expressions are given in Eqs. (8) and (9).

$$K_I = [cos^2(\phi/2)]\mathrm{K}_\infty \tag{8}$$

and

$$K_{II} = [sin(\phi/2)cos^2(\phi/2)]\mathrm{K}_\infty \tag{9}$$

where K_∞ is the applied incremental stress intensity factor and ϕ is the angle of deflection. The toughening from deflection due to pure tilting is relatively small, except in conditions of high angle of tilt (>45°). When the crack growth phenomenon is entirely due to K_I, Eq. (8) can be reorganized in Eq. (10) to obtain the toughening ratio (λ_d).

$$\lambda_d = \frac{\mathrm{K}_\infty}{\mathrm{K}_o} = \frac{1}{cos^2(\phi/2)} \tag{10}$$

where K_o is the intrinsic stress intensity factor. Furthermore, the toughening ratio can be rewritten as:

$$\lambda_d = \frac{\mathrm{K}_\infty}{\mathrm{K}_o} = \frac{\mathrm{K}_\mathrm{D} + \mathrm{K}_o}{\mathrm{K}_o} \tag{11}$$

where K_D is deflection-induced toughening and can be rearranged as follows:

$$K_D = \lambda_d K_o - K_o = (\lambda_d - 1)K_o \tag{12}$$

Finally, the overall fracture toughness of the composite (K_C) is estimated using Eq. (13).

$$K_C = K_i + K_D = K_i + \left[\frac{1}{cos^2(\phi/2)} - 1\right] K_o \tag{13}$$

3.1.3. *Linear superposition of toughening mechanisms*

The concept of linear superposition is used to estimate the combined contributions of the toughening mechanisms to the composite's toughness. Possible interactions between individual toughening conditions are neglected. The superimposed toughening (K_{SC}) due to SSB and crack deflection is given by Eq. (14):

$$K_{SC} = K_i + \alpha V_f \sqrt{\frac{2}{\pi}} \int_0^L \frac{\sigma_y}{\sqrt{x}} dx + \left[\frac{1}{cos^2(\phi/2)} - 1\right] K_o \tag{14a}$$

or

$$K_{SC} = K_i + \Delta K_{SSB} + \Delta K_D \tag{14b}$$

Similarly, Eq. (15) shows the toughening superposition from LSB and crack deflection:

$$K_{SC} = K_i + \alpha V_f \int_L^{\cdot} \sigma_y h(a,x) dx + \left[\frac{1}{cos^2(\phi/2)} - 1\right] K_o \tag{15b}$$

or

$$K_{SC} = K_i + \Delta K_{LSB} + \Delta K_D \tag{15b}$$

4. Results and discussion

4.1. *Microstructure*

The mycelium morphologies observed under optical microscopy and SEM are presented in Fig. 3. Fig. 3a shows the network microstructure of the growing pure mycelium in a culture slant. As described above, each hypha filament elongates outward fusing with other growing filaments to form a large fractal network structure [1]. Fig. 3b shows a dense network of deactivated mycelium filaments. Image analysis of multiple SEM micrographs was performed to estimate the average hypha filament diameter. The corresponding size distribution is illustrated in Fig. 3c and the mean diameter is 1.19 ± 0.5 μm.

The microstructural cross-section of the different samples with varying laterite proportions are presented in Fig. 4. A corresponding decrease in the mycelium density is observed with increasing laterite

Table 3
Summary of Fett and Munz SENB specimen parameters subjected to weighted crack bridging fractions [38].

ν	μ				
	0	1	2	3	4
0	0.4980	2.4463	0.0700	1.3187	−3.067
1	0.5416	−5.0806	24.3447	−32.7208	18.1214
2	−0.19277	2.55863	−12.6415	19.7630	−10.986

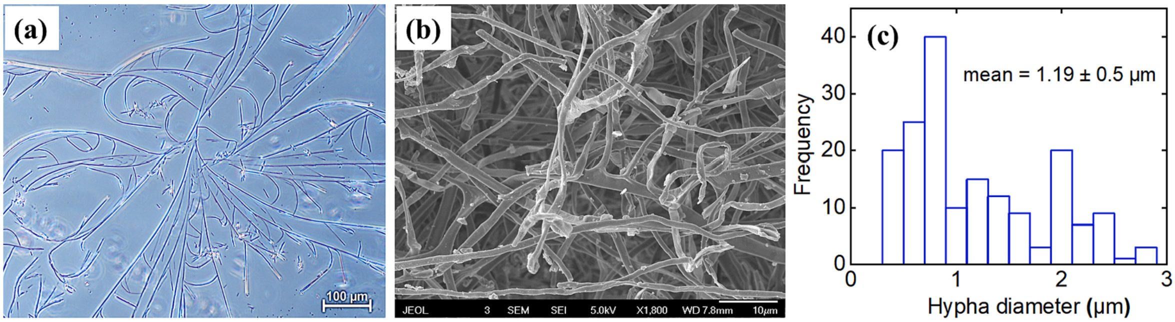

Fig. 3. Morphological characterization of mycelium: (a) optical image of living mycelium in a culture medium (b) SEM image of mycelium network (c) hyphae size distribution with mean diameter of 1.19 ± 0.5 µm.

composition. The laterite particles function as stiffening inclusions and not nutritional source. The mycelium forms a consistent binding matrix in samples with laterite content below 20 wt%, Fig. 4a–c. Poor mycelium growth and reduced density is observed in samples with increased laterite content from 20 to 60 wt%, Fig. 4d–e. The deterioration in the mycelial growth is more pronounced in samples with laterite content exceeding 60 wt%, Fig. 4f. The effect of the mycelium as a binder is significantly reduced.

4.2. EDS analysis of laterite particles

EDS elemental distribution maps and point analysis spectrum of the laterite particles are presented in Fig. 5. The EDS analysis of the soil indicated the presence of O, Si, Al, Pb, Fe, and C. The result reveals that the material stiffness due to the laterite particles is strongly associated with C, Al, Si, and O. This suggests the formation of cementitious hydrates such as calcium silicate hydrate and calcium aluminum hydrate under high pH conditions created by the mycelium biological activities. These hydrates significantly increase the stiffness and strengths of the composites as reported in our earlier study [1]. Badreddine et al. [44], Islam et al. [45], and Moon et al. [46] reported similar findings, stating that the hydrates are primarily responsible for increased stiffness. Thus, the significance of adding the laterite particles was their ability to control the stiffness and compressive strength of the resulting composites, in our previous study. The laterite particles also have the potential to control the underlying toughening and fracture mechanisms, as their weight fractions are varied, in this study.

4.3. Resistance-curve behavior

The measured resistance-curve behavior for each tested specimen showing the toughening increment over the intrinsic level is presented in Fig. 6**.** The calculated information from the resistance curves are quantified in Table 4 and illustrated in Fig. 7. These include the initiation, steady-state, and fracture stress intensity factors (K_O, K_{SS}, and K_Q, respectively), toughening increment (ΔK), and critical notch length-to-width ratios (a_C/W).

The crack initiation stress intensity factor was measured over a range of 0.14 (MHC–20) to 0.17 MPa $\sqrt{m}$ (MHC–0). The average critical crack growth varied from an a_c/W ratio of 0.54 to 0.81 mm. The critical stress intensity factor (K_Q) varied approximately from 0.165 (MHC–70) to 0.25 MPa $\sqrt{m}$ (MHC–0). The toughening increment was calculated to be highest in MHC–0 (0.087 MPa $\sqrt{m}$) and lowest in MHC–70 (0.02 MPa $\sqrt{m}$).

The initial slope of the R-curve ($\Delta K/\Delta a$) was measured to be steep in all samples, Fig. 6a–f. However, the slopes in MHC–0 and MHC–10 are very steep, because they are predominantly a function of the parameters $1/x^{\ 1/2}$ and h(a, x) associated with crack bridging from section 3, Fig. 6a–b. The slope steepness in MHC–20 and MHC–40 is proportional to a partial contribution from $1/x^{\ 1/2}$ and h(a, x) as well as $1/cos^2(\phi/2)$. A reduced steepness from the crack bridging and crack deflection is observed, Fig. 6d–e. In both cases, evidence of transverse bridging ligaments are observed from *in-situ* imaging of the sample side profiles, Fig. 8a–d, and the bridging is observed to occur before the peak load. Crack-bridging phenomena is further discussed in section 4.8.

However, the slopes are shallower in MHC–60 and MHC–70 which are a function of $1/cos^2(\phi/2)$ associated with crack deflection, Fig. 8e–f. Generally, the curves then plateau into a steady state domain which is attributed to the condition in which the rate of fracture of the bridging ligaments (behind the crack tip) is balanced by the crack extension and the formation of new bridging ligaments (ahead of the initial crack tip), [28]. This domain occurs in the Δa range of ~ 1.5–2.5 mm, Fig. 6a–f.

Then, finally, the curves undergo critical crack conditions in which there is rapid crack growth exceeding the shielding effects. Certain anomalies were observed in some specimens which are attributed to the influence of the specimen boundary and fracture process zone [33]. Hence, a limiting factor ($a_c/w \leq 0.65$) and a small crack-bridging zone were maintained to ensure plain strain conditions for the resistance curve behavior [47].

4.4. Fracture toughness

The fracture toughness measurements of the mycelium-hemp composites are presented in Fig. 7. The critical values of the stress intensity at fracture (K_{IC}) are re-presented. The calculated toughness is based on the critical value of the stress intensity factor for which $P_{max} < 1.1\ P_Q$. The highest fracture toughness ($0.25\ MPa\sqrt{m}$) is measured in MHC–0 (Fig. 6a) and a systematic decrease is observed with increasing laterite proportions. Similar results have been reported by Agopyan and John [48] and Savastano et al. [49]. They observed that higher fiber volume fraction corresponds to increased fracture toughness in vegetable fiber-reinforced cementitious composites.

4.5. Comparison of toughening predictions with measured results

The predictions obtained from the analytical models are compared with the measured resistance-curves and are presented in Fig. 6. Parameters such as the bridging fiber volume (V_f) and the bridge length (L) are extracted from the image analysis of the side profiles presented in Fig. 8. Similarly, the local deflection angles (ϕ) for crack-deflection toughening predictions are quantified from the crack deflection profiles [50], extracted from Fig. 8.

The SSB and LSB model predictions capture the general trends of the resistance-curve behavior, reproducing the experimental curves. However, from the SSB prediction, the overall toughening increment (ΔK_{SSB}) is an overestimation of the experimental values. This is pronounced in domain with crack length exceeding 0.5 mm (Fig. 6a–d). This is consistent with results reported by Mustapha et al. [51]. In the case of the LSB model, the predictions provide a closer approximation of the experimental data (Fig. 6a–d). The LSB model also captures the load re-

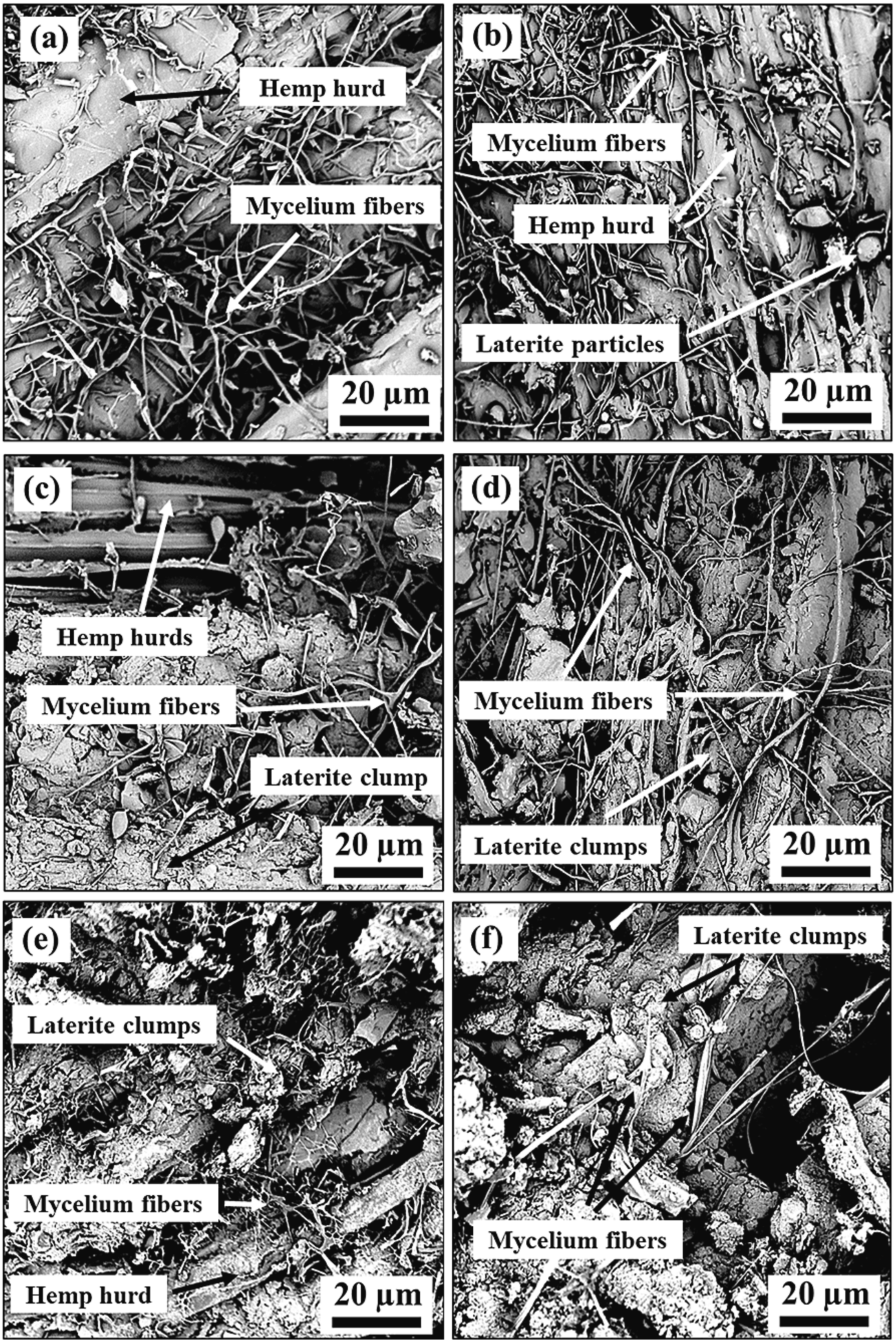

Fig. 4. Morphological characterization of mycelium-hemp composite showing mycelial density variation in the different samples: (a) MHC–0 (b) MHC–10 (c) MHC–20 (d) MHC–40 (e) MHC–60 (f) MHC–70.

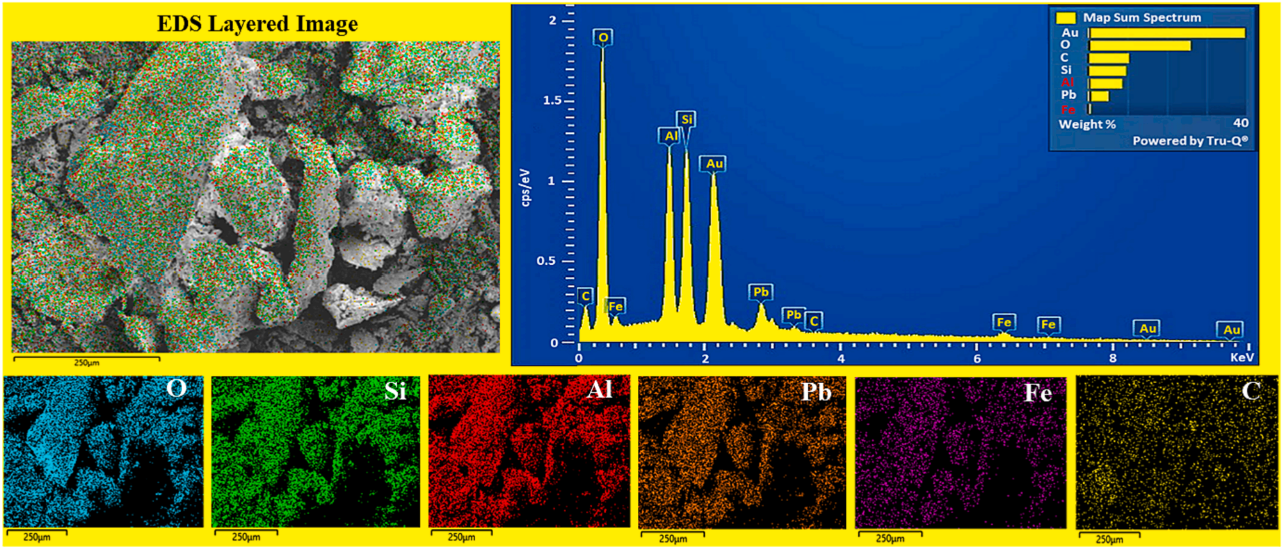

Fig. 5. Microscopy and spectroscopy examination of laterite particles. Secondary electron image (top left), EDS spectrum (top right), and x-ray elemental maps (bottom) of laterite particles. The specimens were coated with Au/Pd (60:40), hence the Au and Pd peaks in the EDS spectrum.

distribution that occurs along the bridging zone, as the crack length increases. It also accounts for the fracture of the bridging ligaments and the consequent redistribution of stress associated with such fracture. In contrast, the SSB model assumes no fiber cracking. A uniform stress distribution is also assumed to occur across the crack bridging zone. This explains why the SSB overestimates the resistance-curve behavior.

In the case of the deflection model, the toughening effects due to pure tilting are relatively small and dependent on the tilting angles. The deflection model is limited in reproducing the measured resistance-curve in samples with low laterite contents. However, in samples with high laterite content, the crack deflection model approximates the measured curves (Fig. 6e–f). In samples with high laterite weight fractions (MHC–60 and MHC–70), initial crack length could not be measured due to crack propagation instability. Crack shielding due to bridging is negligible, Fig. 6e–f. Consequently, the SSB and LSB curves could not be obtained.

The linear superposition of the multiple toughening mechanisms estimated the combined effects of the individual prediction models. Though this neglects the possible interaction between the individual toughening mechanisms, it provides the closest prediction to the experimental data (Fig. 6a–d).

4.6. *Fracture modes*

Observations of the fractured surfaces of the SENB test specimens provide valuable information on the mechanisms of fracture. The representative images of the fracture surfaces of the composites are shown in Fig. 9. In MHC–0, MHC–10, and MHC–20 samples, there were varying incidences of pulled-out fibers and associated voids left on the opposite surfaces of fracture (Fig. 9a–c). These behaviors are related to higher toughness and greater ductility levels, prior to final fracture. The fractured surfaces also show evidence of hemp hurds splitting and mycelium matrix incrustations, indicating a combined transgranular and intergranular fracture mechanisms. Whereas, in samples with higher laterite weight percentages (40–70 wt%), there is evidence of transgranular debonding and decreased mycelium incrustations. These suggest reduced interactions between the mycelium matrix and the hemp hurds as well as the laterite particles, as illustrated in Fig. 9d–f.

4.7. *Toughening mechanisms*

In-situ observations and schematics of the toughening mechanisms displayed by mycelium-hemp composite are presented in Fig. 10. The initiation toughness of each sample occurs at local domain of high ductility, the mycelium-rich regime. Laterite particles lower the initiation toughness due to crack growth instability at the crack tip. Increase in the laterite content results in additional stress concentration effects at the crack front [28]. This explains the variation observed in the initiation toughness of the different samples presented in Fig. 6.

Beyond the initiation toughness, two different toughening mechanisms were predominant, depending on the proportion of laterite particles. In samples with low laterite content (MHC–0 and MHC–10), toughening due to crack bridging was dominant, Fig. 10a and b. However, in MHC–20 and MHC–40 samples, the toughening is due to local crack deflection and some amounts of crack bridging (Fig. 10c and d). However, as the laterite proportion further increases in MHC–60 and MHC–70 samples, the dominant toughening mechanism is by crack deflection (Fig. 10d and e). The crack microstructural interaction reveals that the fiber is a more ductile component and difficult crack path. Hence, at higher volume of mycelium ligaments, the crack propagation pathway is more constrained. The bridging ligaments therefore undergo constrained yielding before breaking which offers more toughening.

4.8. *Crack-microstructure interactions*

The crack-microstructure interactions and damage phenomena sequence observed in the single-edge notched fractured experiments are presented in Fig. 11. The crack interactions are of two types, depending on the laterite content. In both types, microcracks initiate from the notch tip at a critical crack driving force. In samples with low laterite content, growing cracks (from the notch tip) are associated with interfacial delamination at the mycelium–hemp interface, and loop around the hemp hurds. This results in debonding and radial cracking, as shown in Fig. 11a. However, in samples with high laterite content (type 2 samples), crack instability is observed beyond the notch tip causing multiple microcrack initiations around the laterite particles (Fig. 11b). At higher crack driving forces, microcracks formed due to stress concentration effects develop into macrocracks.

Progressively, as crack propagates in samples with low laterite content, stress concentration builds up around the hemp hurds. This initiates longer cracks ahead, leaving the mycelium fibers bridging the crack behind. As the bridging length increases, the stresses on the bridging ligaments get higher and the components begin to crack (Fig. 11a). The effective bridge length keeps shifting forward as long as the crack

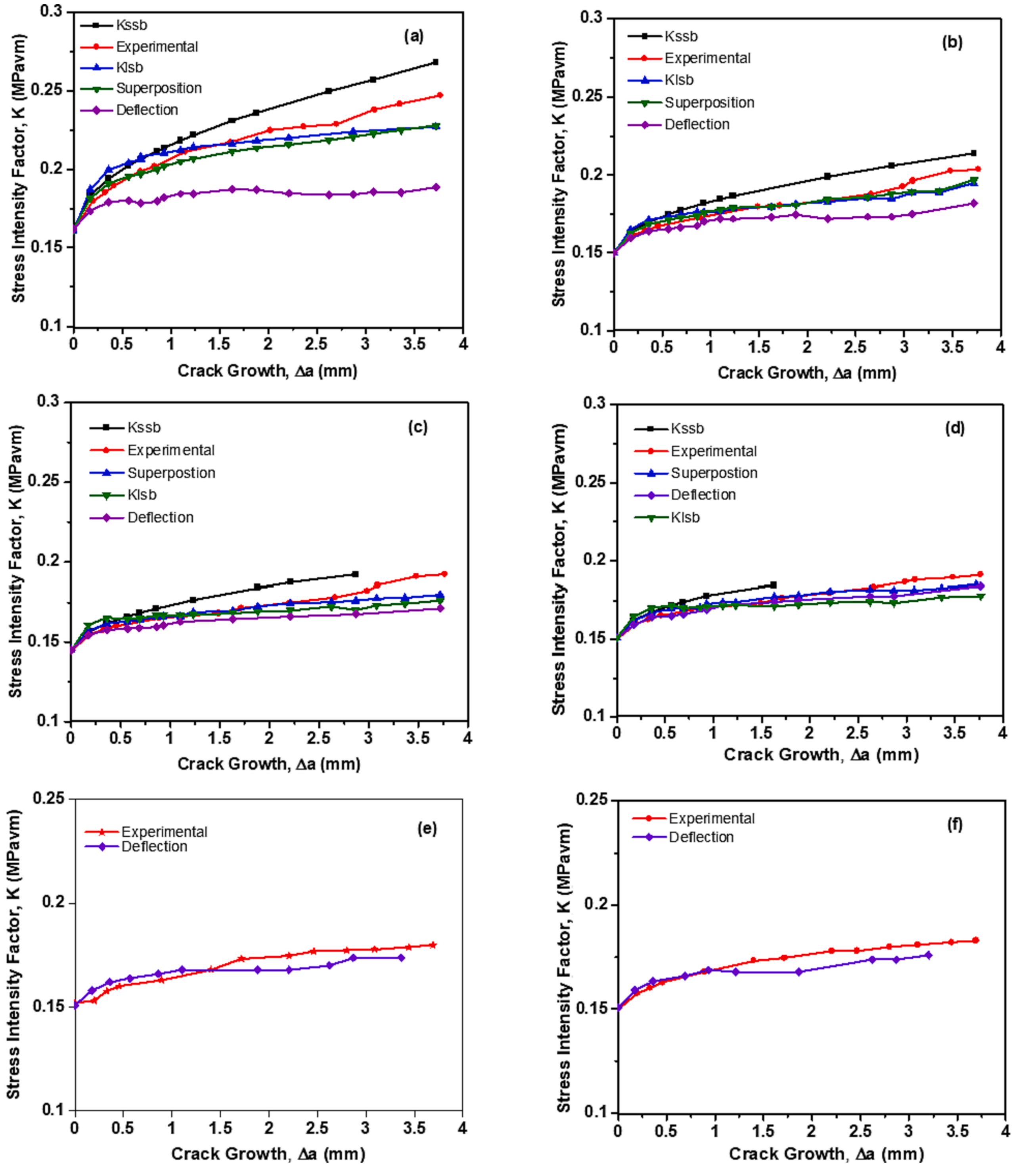

Fig. 6. Experimental and predicted resistance-curves of mycelium-based composites. The predictions are based on small-, large-scale bridging, and deflection models: (a) MHC–0 (b) MHC–10 (c) MHC–20 (d) MHC–40 (e) MHC–60 (f) MHC–70.

opening displacement is sufficient to load the bridging ligaments to failure. This further explains why the LSB model is a better prediction of the resistance-curve behavior than the SSB. However, in samples with high laterite content, the macrocrack rapidly propagates through the brittle laterite interfaces of the composite, resulting in interfacial fracture (Fig. 11b).

4.9. Implications

This research provides new insights into the effects of laterite reinforcement on the toughening mechanisms of mycelium-hemp composites. The findings of this work show that the composite toughening is significantly influenced by the role of the mycelium either as a dominant material or as a natural glue. When the mycelium is a dominant component, the crack growth is intercepted by the fibers and that provides attractive toughening by crack bridging.

Table 4
Main information from the measured resistance-curve behaviors of mycelium-hemp composites.

Sample	Specimen No.	K_o[a]	K_{ss}	K_Q	ΔK	a_c/W
MHC-0	1–1	0.16	0.235	0.247	0.087	0.54
	1–2	0.155	0.221	0.29	0.09	0.65
	1–3	0.161	0.219	0.245	0.084	0.62
	1–4	0.17	0.225	0.27	0.06	0.55
MHC-10	2–1	0.15	0.16	0.21	0.06	0.63
	2–2	0.145	0.175	0.2	0.055	0.60
	2–3	0.165	0.185	0.195	0.047	0.57
	2–4	0.155	0.2	0.205	0.045	0.55
MHC-20	3–1	0.136	0.16	0.192	0.056	0.62
	3–2	0.15	0.145	0.2	0.05	0.58
	3–3	0.16	0.18	0.214	0.04	0.54
	3–4	0.14	0.175	0.19	0.05	0.62
MHC-40	4–1	0.151	0.17	0.19	0.039	0.63
	4–2	0.16	0.157	0.193	0.033	0.54
	4–3	0.12	0.12	0.380[b]	0.260[b]	0.79[b]
	4–4	0.145	0.175	0.185	0.04	0.65
MHC-60	5–1	0.156	0.15	0.182	0.026	0.63
	5–2	0.122	0.173	0.35[b]	0.228[b]	0.81[b]
	5–3	0.15	0.17	0.185	0.035	0.60
	5–4	0.155	0.175	0.17	0.015	0.61
MHC-70	6–1	0.155	0.146	0.178	0.023	0.58
	6–2	0.145	0.165	0.165	0.02	0.64
	6–3	0.135	0.193	0.358[b]	0.223[b]	0.78[b]
	6–4	0.15	0.175	0.18	0.03	0.60

$K_o, K_{ss}, K_Q, \Delta K$: unit is in MPa $\sqrt{m}$.

[a] $a_O/W \sim 0.45$.

[b] Values are not considered representative of the intrinsic behavior of the composite.

Whereas, when the mycelium functions only as a glue in composites with high laterite content, its crack bridging capability is significantly reduced. Alternatively, the laterite particles promote crack deflection which offers minimal toughening. At high laterite contents, the cracks typically deflect around the local boundaries of the laterite particles. This gives some modest deflection toughening but not as much toughening from bridging conditions. This understanding provides valuable insight to design mycelium-based composites with tunable range of material toughness.

The resistance-curve experiments and the analytical predictions of the fracture mechanics provide valuable information about the effect of granular particles on the mechanical properties of mycelium-based composites. Our earlier study [1] shows that compressive strength is effectively increased with laterite particle inclusion. However, this work reveals that fracture toughness is inversely proportional to weight fractions of laterite particles. This offers useful insights into the design of mycelium-based composites with tunable properties for multifunctional applications. However, the potential applications the biocomposites are still limited to non-load bearing and indoor structures such as pavilions, cubicles, partition walls, and ceiling tiles [52]. The authors now state clearly that future work should focus on the use of cohesive zone models in the modelling of crack bridging.

To realize the full potential of mycelium-based composites for structural applications, more research is needed for improved post-processing strategies and the toughening of these materials. Furthermore, future work should focus on the use of more recent modeling approaches such as cohesive zone fracture models to provide more thorough analysis of fracture mechanics to elucidate the process of crack opening across extending crack tips.

5. Summary and concluding remarks

This study uses a combination of experiments and models to explore the fracture and toughening of mycelium-based composites. The bio-processed mycelium blocks, comprising cellulose hemp-ducts as reinforcing and nutritional substrates, are intertwined with increasing proportions of laterite particles. Single-edge notch specimens are tested to explore the effects of varying laterite content on the resistance-curve behavior of the composites. The measured toughening mechanisms and analytical predictions provide new insights for the design of functional materials with tunable ranges of fracture toughness. They also provide a mechanism-based framework for the microstructural design of myce-

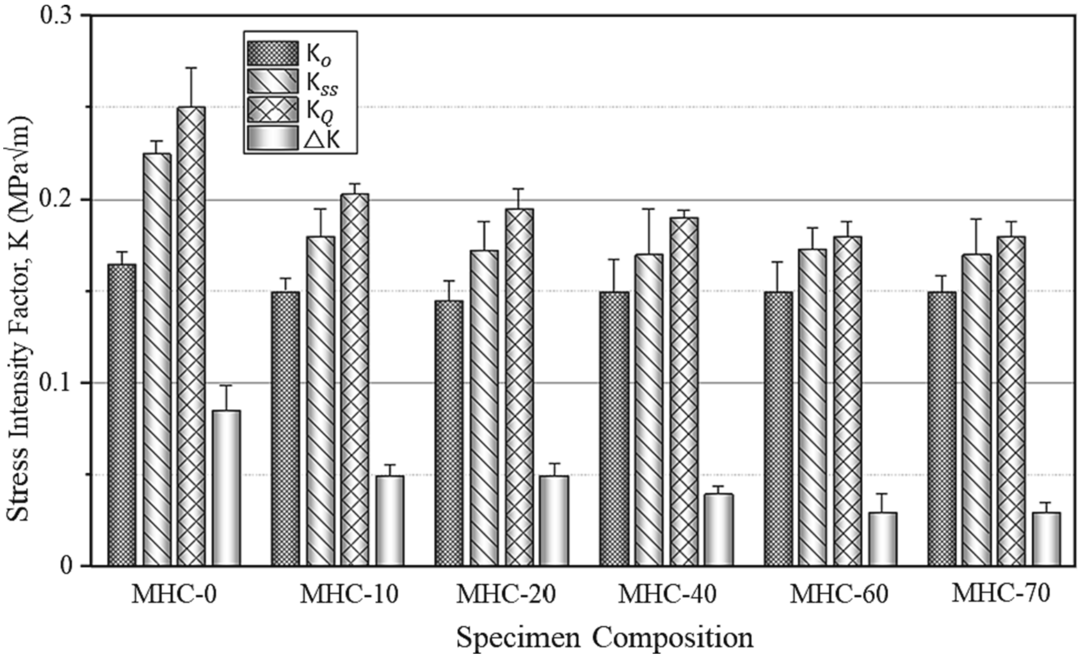

Fig. 7. Chart of the main information from the measured resistance-curve behavior of mycelium-hemp composites with varying weight fractions of laterite particles.

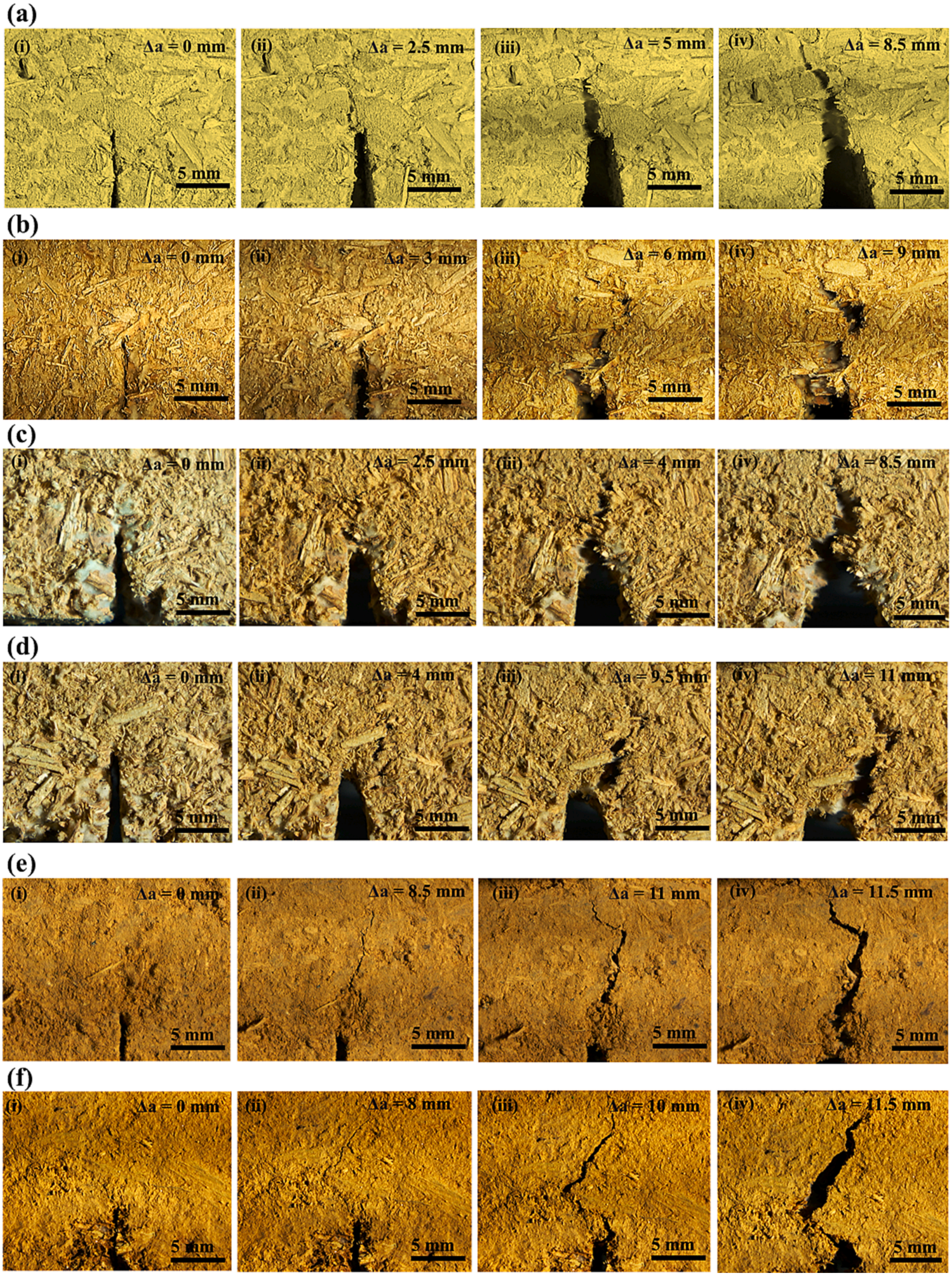

Fig. 8. Optical images of *in-situ* observations of crack propagation from single edge notched fracture toughness experiments: (a)–(d) MHC–0, –10, –20, and –40 (i) initial notch, (ii) transgranular cracks with bridging segments, (iii) elongated unstable crack opening, (iv) increased crack opening and deflected crack profiles with bridging ligaments; (e)–(f) MHC–60 and –70 (i) initial notch, (ii) intergranular brittle and initial deflected cracks, (iii) unstable crack opening and further crack deflections, (iv) increased crack opening and pronounced crack deflection profiles.

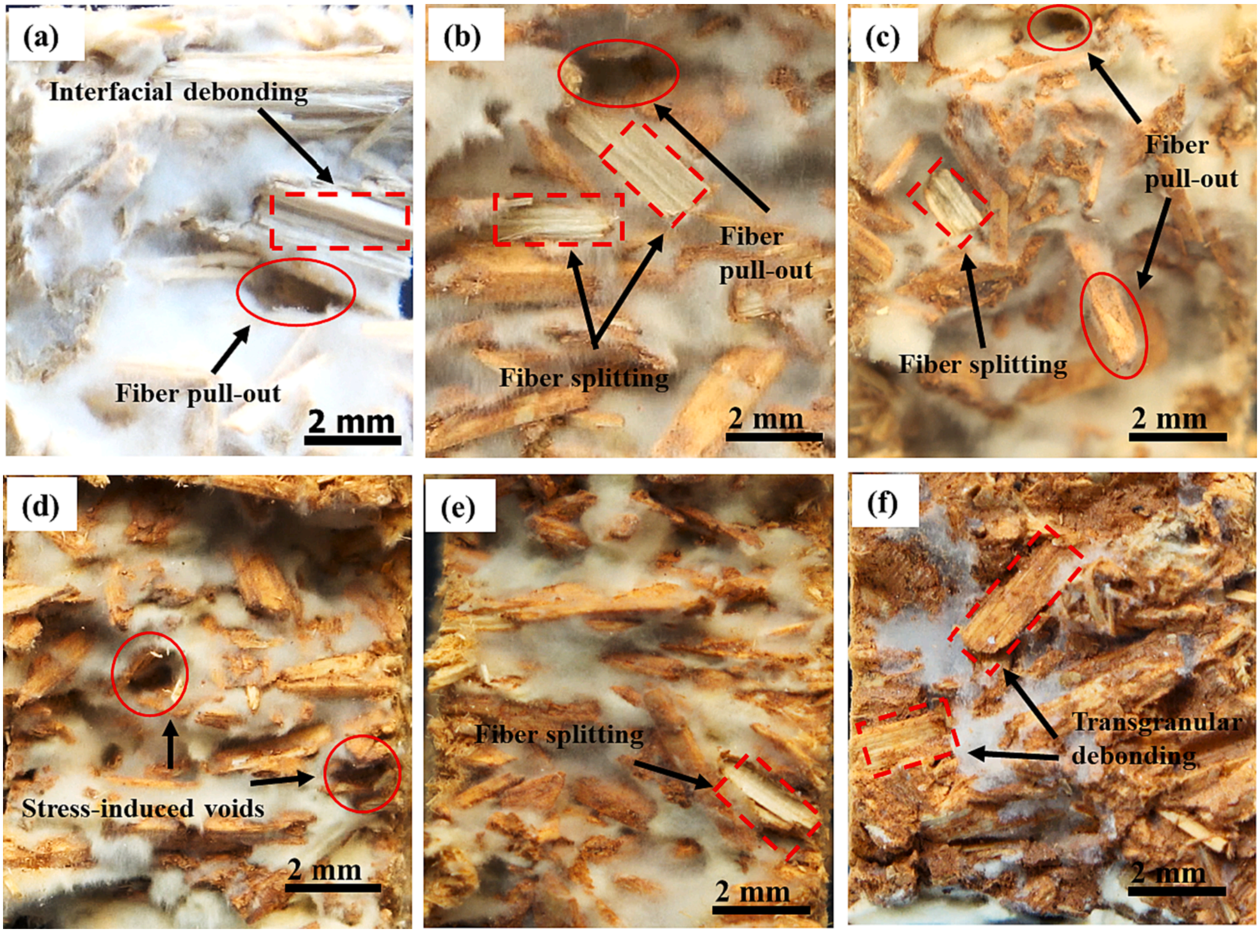

Fig. 9. Optical images of fractured surface from SENB experiments: (a) MHC–0 (b) MHC–10 (c) MHC–20 (d) MHC–40 (e) MHC–60 (f) MHC–70. Evidence of fiber pull out is indicative of good adhesion from mycelium matrix incrustations.

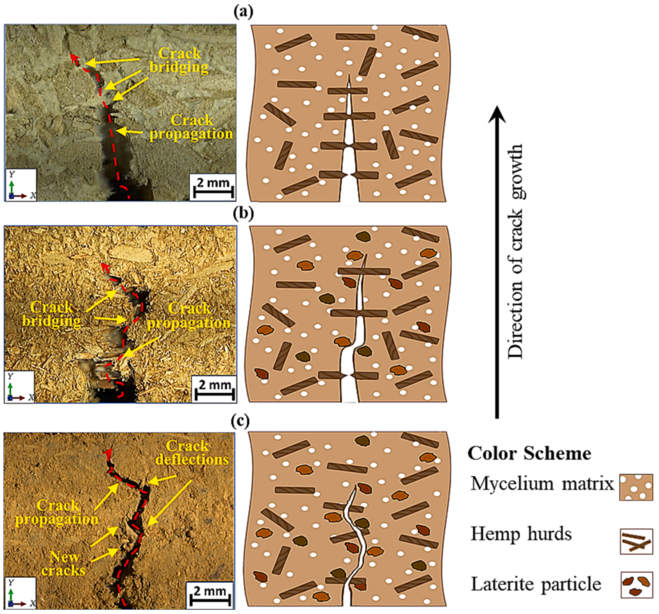

Fig. 10. *In-situ* observations (left) and schematic illustrations (right) of toughening mechanisms observed in mycelium-hemp composites with varying proportions of laterite particles (a) 0–20 wt% (b) 20–40 wt% (c) 60–70 wt%. The white dots in brown-colored background, the randomly distributed rods, and the irregular shapes illustrate the mycelium matrix, the hump hurds, and the laterite particles, respectively.

lium and mycelium-laterite composites for potential applications in sustainable buildings. Salient conclusions arising from this study are summarized below:

1. Toughening is dominated by crack-bridging at low-weight fractions of laterite (<20 wt%). A combination of crack-bridging and crack deflection is observed to occur at increased laterite weight fractions (20–40 wt%). However, toughening is shown to occur predominantly by crack deflection at higher weight percentages (>40 wt%).
2. The overall toughening in the composites is predicted by the superposition of the observed crack-tip shielding from crack bridging and crack deflection, for samples with weight percentages of laterite up to 60 wt%. Above this laterite fraction, toughening due to deflection occurs predominantly by crack tilting around the laterite particles.
3. Fracture toughness of 0.17 and 0.25 MPa $\sqrt{m}$ were measured in MHC–0 and MHC–70, respectively. The higher toughness can be considered acceptable for fabrication of thin panels and tiles for internal applications [52].
4. The fractographic analysis of samples with laterite weight proportions below 20 wt% indicates a combination of transgranular and intergranular fractures. Whereas the fracture mode of samples with higher weight percentages (≥40 wt%) predominantly constitutes intergranular brittle fracture.

CRediT authorship contribution statement

Precious O. Etinosa: Writing – original draft, Writing – review & editing, Validation, Methodology, Investigation, Formal analysis,

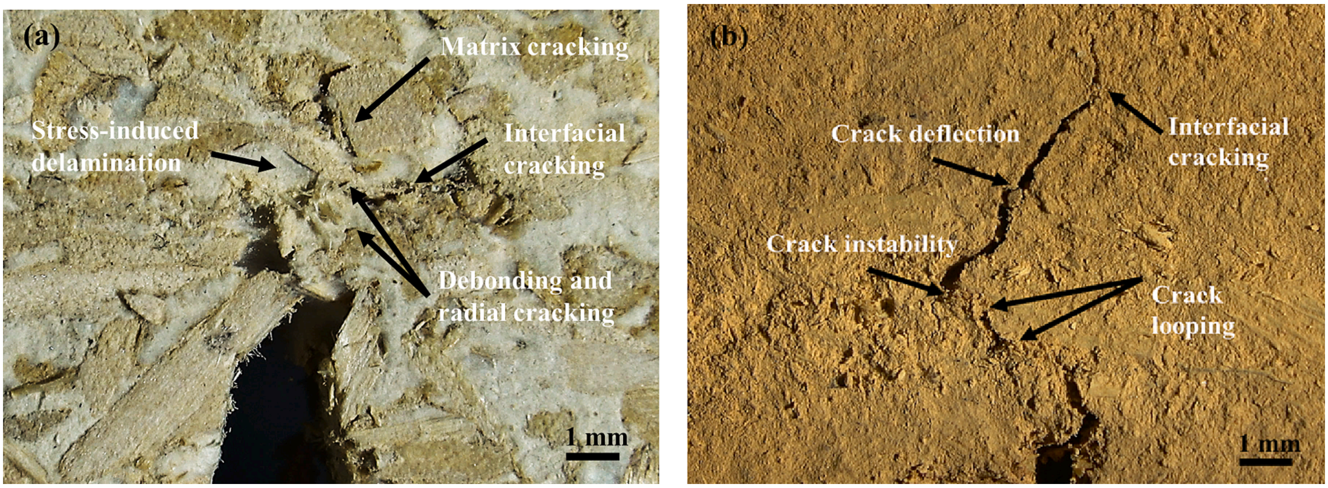

Fig. 11. Optical images of the microstructural interactions in (a) mycelium-hemp composite showing crack interaction at the bridging ligaments and (b) mycelium-hemp composite stiffened with laterite particles.

Conceptualization. **Ali A. Salifu:** Conceptualization, Formal analysis, Investigation, Supervision, Writing – review & editing. **Sarah Osafo:** Methodology, Investigation, Formal analysis. **Stanley C. Eluu:** Data curation, Visualization, Writing – review & editing. **John D. Obayemi:** Conceptualization, Investigation, Validation, Writing – review & editing. **Winston O. Soboyejo:** Writing – review & editing, Supervision, Resources, Formal analysis, Conceptualization.

Declaration of competing interest

The authors declare that they have no known competing financial interests or personal relationships that could have appeared to influence the work reported in this paper.

Data availability

Data will be made available on request.

Acknowledgments

The authors are grateful for the financial support from World Bank African Centers of Excellence (ACE) program (Grant No. PAMI P126974) and the Worcester Polytechnic Institute, Worcester, USA.

References

[1] P.O. Etinosa, et al., Self-organized mycelium biocomposites: Effects of geometry and laterite composition on compressive behavior, J. Mech. Behav. Biomed. Mater. 142 (2023), 105831, https://doi.org/10.1016/j.jmbbm.2023.105831.

[2] M. Haneef, L. Ceseracciu, C. Canale, et al., Advanced Materials from Fungal Mycelium: Fabrication and tuning of physical properties, Sci. Rep. 7 (2017) 41292, https://doi.org/10.1038/srep41292.

[3] A. Shalwan, B.F. Yousif, In state of art: Mechanical and tribological behavior of polymeric composites based on natural fibers, Mater. Des. 48 (2013) 14–24, https://doi.org/10.1016/j.matdes.2012.07.014.

[4] M. Epicoco, Patterns of innovation and organizational demography in emerging sustainable fields: An analysis of the chemical sector, Res. Policy 45 (2016) 427–441, https://doi.org/10.1016/j.respol.2015.10.013.

[5] L. Ceseracciu, et al., Robust and Biodegradable Elastomers Based on Corn Starch and Polydimethylsiloxane (PDMS), ACS Appl. Mater. Interfaces 7 (6) (2015) 3742–3753, https://doi.org/10.1021/am508515z.

[6] B. Sizirici, et al., A review of carbon footprint reduction in construction industry, from design to operation, Materials 14 (20) (Oct. 2021) 6094, https://doi.org/10.3390/ma14206094.

[7] Y. Lu, X. Zhu, Q. Cui, Effectiveness and equity implications of carbon policies in the United States construction industry, Build. Environ. 49 (Mar. 2012) 259–269, https://doi.org/10.1016/j.buildenv.2011.10.002.

[8] A. Livne, H.A.B. Wösten, D. Pearlmutter, E. Gal, Fungal mycelium bio-composite acts as a CO 2-sink building material with low embodied energy, ACS Sustain. Chem. Eng. 10 (37) (2022) 12099–12106, https://doi.org/10.1021/acssuschemeng.2c01314.

[9] G.A. Holt, G. McIntyre, D. Flagg, E. Bayer, J.D. Wanjura, M.G. Pelletier, Fungal mycelium and cotton plant materials in the manufacture of biodegradable molded packaging material: evaluation study of select blends of cotton byproducts, J. Biobaased Mater. Bioenergy 6 (4) (2012) 431–439, https://doi.org/10.1166/JBMB.2012.1241.

[10] C. Vilela, et al., The quest for sustainable polyesters-insights into the future, Polym. Chem. 5 (2014) 3119–3141, https://doi.org/10.1039/c3py01213a.

[11] R. A. J. Verlinden, D. J. Hill, M. A. Kenward, C. D. Williams, I. Radecka, Bacterial synthesis of biodegradable polyhydroxyalkanoates’, J. Appl. Microbiol.. 102, 6, 1437-1449, doi: 10.1111/j.1365-2672.2007.03335.x.

[12] J.G. Hardy, L.M. Rö, T.R. Scheibel, Polymeric materials based on silk proteins, Polymer 49 (2008) 4309–4327, https://doi.org/10.1016/j.polymer.2008.08.006.

[13] M. Râpă, E.E. Popa, Biopolymers for edible films and coatings in food applications, Handbook Biopolym. (2023) 1085–1115, https://doi.org/10.1007/978-981-19-0710-4_40.

[14] O.A. Osuchukwu, A. Salihi, I. Abdullahi, P. Osayamen Etinosa, D.O. Obada, Weibull modulus of a novel mixture of natural hydroxyapatite materials produced from biowastes, Results Mater. 18 (2023) 2590–2638, https://doi.org/10.1016/j.rinma.2023.100394.

[15] O.A. Osuchukwu, A. Salihi, I. Abdullahi, P. Osayamen Etinosa, D.O. Obada, A comparative study of the mechanical properties of sol-gel derived hydroxyapatite produced from a novel mixture of two natural biowastes for biomedical applications, Mater. Chem. Phys. 297 (2023), 127434, https://doi.org/10.1016/j.matchemphys.2023.127434.

[16] A.K. Mohanty, M. Misra, G. Hinrichsen, Biofibers, biodegradable polymers and biocomposites: An overview, Macromol. Mater. Eng. 276, 277 (2000) 1–24, 10.1002/(SICI)1439-2054(20000301)276:1<1:aid-mame1>3.0.co;2-w.

[17] M. Irimia-Vladu, “Green” electronics: biodegradable and biocompatible materials and devices for sustainable future, Chem. Soc. Rev. 43 (2) (2014) 588–610, https://doi.org/10.1039/C3CS60235D.

[18] N. Attias, A. Livne, T. Abitbol, State of the art, recent advances, and challenges in the field of fungal mycelium materials: a snapshot of the 2021 Mini Meeting, Fungal Biol. Biotechnol. 8 (2021) 12, https://doi.org/10.1186/s40694-021-00118-3.

[19] P.O. Etinosa, W.O. Soboyejo, Cell/surface interactions and the integrity of Ti-6Al-4V structures: effects of surface texture and RGD coatings, *Compreh. Struct. Integr.*, Elsevier (2023) 35–54, https://doi.org/10.1016/B978-0-12-822944-6.00086-4.

[20] A. R. M Maray, M. K. Mostafa, and A. M. El-Din A El-Fakhrany, ‘Effect of pretreatments and drying methods on physico-chemical, sensory characteristics and nutritional value of oyster mushroom’, J. Food Process. Preserv., 42, 1, e13352, doi: 10.1111/jfpp.13352.

[21] K. Renner, C. Kenyó, J. Móczó, and B. Pukánszky, ‘Micromechanical deformation processes in PP/wood composites: Particle characteristics, adhesion, mechanisms’, Compos. Part A: Appl. Sci. Manuf., 41, 1653-1661, doi: 10.1016/j.compositesa.2010.08.001.

[22] A. Shahzad, Hemp fiber and its composites - A review, J. Compos. Mater. 46 (8) (2012) 973–986, https://doi.org/10.1177/0021998311413623.

[23] A. Célino, S. Fréour, F. Jacquemin, P. Casari, G. Mensitieri, The hygroscopic behavior of plant fibers: a review, Front. Chem. 1 (2013) 43, https://doi.org/10.3389/fchem.2013.00043.

[24] P. Wambua, J. Ivens, I. Verpoest, Natural fibers: can they replace glass in fiber reinforced plastics? Compos. Sci. Technol. 63 (2003) 1259–1264, https://doi.org/10.1016/S0266-3538(03)00096-4.

[25] W. Aiduang, J. Kumla, S. Srinuanpan, W. Thamjaree, S. Lumyong, N. Suwannarach, Mechanical, physical, and chemical properties of mycelium-based composites

produced from various lignocellulosic residues and fungal species, J. Fungi 8 (11) (2022) Nov, https://doi.org/10.3390/jof8111125.
[26] M.R. Islam, G. Tudryn, R. Bucinell, et al., Mechanical behavior of mycelium-based particulate composites, J. Mater. Sci. 53 (2018) 16371–16382, https://doi.org/10.1007/s10853-018-2797-z.
[27] N. J. R. P. D. C. Travaglini S, 'Mycology matrix composites', in Proceedings of the American Society for Composites—28th technical conference, State College, 2013, pp. 1–20.
[28] W.O. Soboyejo,' Mechanical properties of engineered materials', Mechanical engineering (Marcel Dekker, Inc.); 152, 2003, ISBN: 0824789008.
[29] P. Kothiyal, A. Joshi, K.K.S. Mer, et al., Influence of Al_2O_3 and Si_3N_4 nanoparticulates on fracture toughness behavior of sintered aluminum, Trans. Indian Inst. Met. 75 (2022) 199–215, https://doi.org/10.1007/s12666-021-02411-6.
[30] American Society for Testing and Materials, 'Standard Test Method for Plane-Strain Fracture Toughness of Metallic Materials, E399-90', 1997.
[31] K.M. Conway, et al., Increasing fracture toughness via architected porosity, Mater. Des. 205 (2021), https://doi.org/10.1016/j.matdes.2021.109696.
[32] B. Budiansky, J.C. Amazicki, A.G. Evansi, Small-scale crack bridging and the fracture toughness of particulate-reinforced ceramics, J. Merh. Phys. Solids 36 (2) (1988) 167.
[33] H. Savastano, A.A. Turner, A.C. Mercer, W.O. Soboyejo, Mechanical behavior of cement-based materials reinforced with sisal fibers, J. Mater. Sci. 6938–6948 (2006), https://doi.org/10.1007/s10853-006-0218-1.
[34] M. Li, W.O. Soboyejo, An investigation of the effects of ductile-layer thickness on the fracture behavior of nickel aluminide microlaminates, Metall. Mater. Trans. A 31 (2000) 1385–1399, https://doi.org/10.1007/s11661-000-0257-1.
[35] H. Gopalan, A. Marshal, M. Hans, et al., On the interplay between microstructure, residual stress and fracture toughness of (Hf-Nb-Ta-Zr)C multi-metal carbide hard coatings, Mater. Des. 224 (2022), https://doi.org/10.1016/j.matdes.2022.111323.
[36] H. Bai, R. Bai, T. Zhao, et al., Multiscale experimental characterization of mode-I interfacial fracture behavior of vitrimer composites, Mater. Des. 112229 (2023), https://doi.org/10.1016/j.matdes.2023.112229.
[37] J. Lou, W.O. Soboyejo, An Investigation of the effects of loading rate on resistance-curve behavior and toughening in cast lamellar gamma-based titanium aluminides, Metall. Mater. Trans. A 32 (2001) 325–337, https://doi.org/10.1007/s11661-001-0264-x.
[38] Fett T. and Munz D, 'Stress Intensity Factors and Weight Functions for One-Dimensional Cracks', Institut fur Materialforschung, 1994, ISSN 0303-4003.
[39] G. Glinka, W. Reinhardt, Weight functions and stress intensity factors for embedded cracks subjected to arbitrary mode I stress fields, Eur. Struct. Integr. Soc. 23 (1999) 183–194, https://doi.org/10.1016/S1566-1369(99)80041-7.
[40] D.R. Bloyer, K.T.V. Rao, R.O. Ritchie, Fracture toughness and R-curve behavior of laminated brittle-matrix composites, Metall. Mater. Trans. A 29 (1998) 2483–2496, https://doi.org/10.1007/s11661-998-0220-0.
[41] B.A. Bilby, G.E. Cardew, I.C. Howard, Stress intensity factors at the tips of kinked and forked cracks, *Anal. Mech.*, Elsevier (1978) 197–200, https://doi.org/10.1016/B978-0-08-022142-7.50039-9.
[42] B. Cotterell, J.R. Rice, Slightly curved or kinked cracks, Int. J. Fract. 16 (2) (Apr. 1980) 155–169, https://doi.org/10.1007/BF00012619.
[43] S. Suresh, Fatigue crack deflection and fracture surface contact: micromechanical models, Metall. Trans. A 16 (1) (Jan. 1985) 249–260, https://doi.org/10.1007/BF02815306.
[44] R. Badreddine, A.-N. Humez, U. Mingelgrin, A. Benchara, F. Meducin, R. Prost, Retention of trace metals by solidified/stabilized wastes: assessment of long-term metal release, Environ. Sci. Tech. 38 (5) (Mar. 2004) 1383–1398, https://doi.org/10.1021/es0209520.
[45] M.N. Islam, X.P. Golam Taki, Y.-T. Nguyen, J.K. Jo, J.-H. Park, Heavy metal stabilization in contaminated soil by treatment with calcined cockle shell, Environ. Sci. Pollut. Res. Int. 24 (8) (2017 Mar) 7177–7183, https://doi.org/10.1007/s11356-016-8330-5.
[46] D. Hyun Moon, et al., Stabilization of lead and copper contaminated firing range soil using calcined oyster shells and fly ash, Environ. Geochem. Health 35 (2013) 705–714, https://doi.org/10.1007/s10653-013-9528-9.
[47] H. Savastano, S.F. Santos, M. Radonjic, W.O. Soboyejo, Fracture and fatigue of natural fiber-reinforced cementitious composites, Cem. Concr. Compos. 31 (2009) 232–243, https://doi.org/10.1016/j.cemconcomp.2009.02.006.
[48] V. Agopyan, V.M. John, Durability evaluation of vegetable fiber reinforced materials, Build. Res. Inf. 20 (4) (Jul. 1992) 233–235, https://doi.org/10.1080/09613219208727212.
[49] H. Savastano, P.G. Warden, R.S.P. Coutts, Brazilian waste fibers as reinforcement for cement-based composites, Cem. Concr. Compos. 22 (5) (Oct. 2000) 379–384, https://doi.org/10.1016/S0958-9465(00)00034-2.
[50] K.T. Faber, A.G. Evans, Crack deflection processes—II. Experiment, Acta Metall. 31 (4) (Apr. 1983) 577–584, https://doi.org/10.1016/0001-6160(83)90047-0.
[51] K. Mustapha, E. Annan, S.T. Azeko, M.G. Zebaze Kana, W.O. Soboyejo, Strength and fracture toughness of earth-based natural fiber-reinforced composites, J. Compos. Mater. 50 (9) (2016) 1145–1160, https://doi.org/10.1177/0021998315589769.
[52] A. Rossi, et al., Home: wood-mycelium composites for CO_2 -neutral, circular interior construction and fittings, IOP Conf. Ser. Earth Environ. Sci. 1078 (1) (Sep. 2022), 012068, https://doi.org/10.1088/1755-1315/1078/1/012068.